

Weld Pool Formation in Keyhole Plasma Arc Welding

Subjects: Engineering, Manufacturing

Contributor: Shinichi Tashiro

The Keyhole Plasma Arc Welding (KPAW) process utilizes arc plasma highly constricted by a water-cooled copper nozzle to produce great arc pressure for opening a keyhole in the weld pool, achieving full penetration to the thick plate. However, advanced control of welding is known to still be difficult due to the complexity of the process mechanism, in which thermal and dynamic interactions among the arc, keyhole, and weld pool are critically important. In KPAW, two large eddies are generally formed in the weld pool behind the keyhole by plasma shear force as the dominant driving force. These govern the heat transport process in the weld pool and have a strong influence on the weld pool formation process. The weld pool flow velocity is much faster than those of other welding processes such as Tungsten Inert Gas (TIG) welding and Gas Metal Arc (GMA) welding, enhancing the heat transport to lower the weld pool surface temperature. Since the strength and direction of this shear force strongly depend on the keyhole shape, it is possible to control the weld pool formation process by changing the keyhole shape by adjusting the torch design and operating parameters. If the lower eddy is relatively stronger, the heat transport to the bottom side increases and the penetration increases. However, burn-through is more likely to occur, and heat transport to the top side decreases, causing undercut. In order to realize further sophistication of KPAW, a deep theoretical understanding of the process mechanism is essential.

Keywords: plasma arc welding ; arc plasma ; keyhole ; weld pool ; interaction ; driving force ; heat transport ; mass transport

1. Introduction

Plasma Arc Welding (PAW) is a type of arc welding process utilizing a non-consumable electrode ^[1]. PAW uses a tungsten electrode like Tungsten Inert Gas Welding (TIGW) to generate an arc discharge between the electrode and the base metal. This arc is cooled by a water-cooled copper nozzle attached to the downstream side of the tungsten electrode and is constricted by the thermal pinch effect ^[2], so that an arc with a high current density can be obtained. Accordingly, the plasma jet is strongly accelerated by the Lorentz force and the plasma temperature is highly increased by Joule heating. The high current density causes strong heat transfer from the arc to the base metal due to electron condensation together with thermal conduction from the high-temperature plasma. Consequently, it is possible to obtain a much higher arc pressure and heat flux to the base metal than TIGW, easily forming deep and narrow penetration. **Figure 1** shows a schematic diagram of PAW.

There are two types of welding modes in PAW, melt-in or conduction mode ^[3] and keyhole mode ^[1], depending on the operating parameters. In the former mode, the current value and the plasma gas flow rate are suppressed to generate an arc having a relatively low arc pressure and heat flux, so that welding without forming a keyhole is performed. The latter is called Keyhole PAW (KPAW). The base metal is partly melted by the high heat flux from the arc, and the weld pool surface is gradually pushed down by the arc pressure to form a blind keyhole in the base metal and then full penetration can be achieved to form an open keyhole. This mode is mainly used for square butt welding using the I-groove.

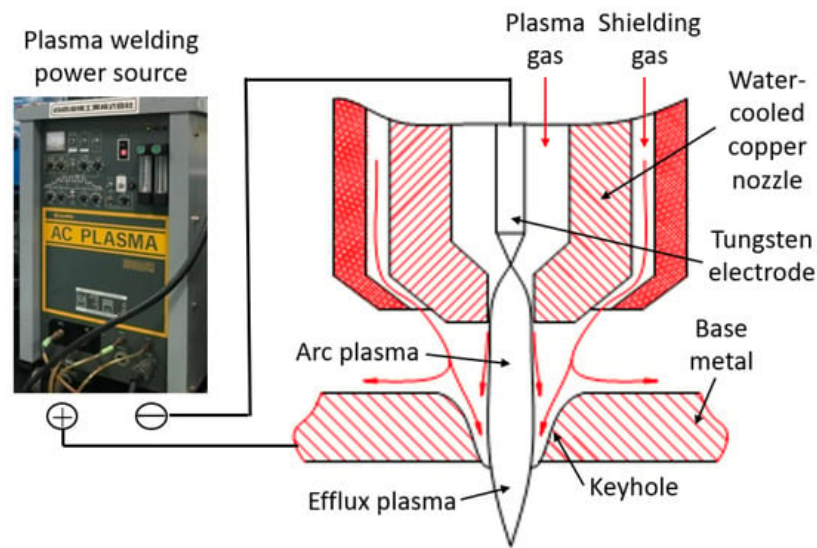


Figure 1. Schematic of plasma arc welding [4].

When welding steel plates, KPAW enables to weld up to a plate thickness of about 6–10 mm in a single welding pass [5]. In the case of Gas Metal Arc Welding (GMAW) of thick plates, a V- or Y-groove is generally applied to the base metal, and several welding passes are required, because of the insufficient penetration ability of GMAW [6]. On the other hand, KPAW generally uses an I-groove, which does not require operation beveling (groove processing), and the welding can be completed in a single welding pass. This enables high-efficiency welding with reduced man-hours and decreases heat input to the base metal, suppressing thermal distortion. Other advantages are that the capital investment is much cheaper than for laser welding and electron beam welding, the tolerance to joint gap of the base metal is large, and also the electrode consumption is small. Due to the many excellent advantages described above, KPAW has a wide range of applications such as structural steel [7], aerospace [8], and automobiles [9].

Much research has been carried out so far with the aim of improving the quality and efficiency of KPAW [10][11][12]. The weld pool formation process of KPAW is strongly influenced by keyhole behavior. In order to guarantee full penetration, it is generally necessary to maintain an open keyhole state with an appropriate keyhole diameter. The keyhole diameter largely depends on the current and the plasma gas flow rate. If these are insufficient, a blind keyhole is formed, making it difficult to obtain full penetration. On the other hand, if both are excessive, the keyhole diameter becomes large. However, the volume of the weld pool increases accordingly, and the width of the weld pool on the bottom surface increases. As a result, the surface tension cannot support the weight of the molten metal, thus leading to a burn-through. Therefore, in order to solve this problem, it is indispensable to develop sensing and control methods for the keyhole during welding.

2. Weld Pool Formation Process

The weld pool formation process is described in this section. During the travel of the torch in the welding direction, the molten metal on the front side of the keyhole is transported through the sides of the keyhole toward the rear region to form the weld pool. The heat transport in the weld pool is considered to be primarily due to weld pool convection, especially in steel welding, driven by the buoyancy force, Lorentz force, Marangoni force, and plasma shear force. Particularly, the shear force and Marangoni force are thought to strongly depend on the keyhole shape, since those work on the surface of the weld pool in the vicinity of the keyhole. The molten metal in the weld pool is supported by the surface tension of the bottom surface of the weld pool, preventing burn-through. As discussed in the previous sections, the arc, keyhole, and weld pool strongly interact together, thus making KPAW a very complex process. Furthermore, the weld pool formation easily becomes unstable, inducing various welding defects, for example, by disturbance or a change in the condition in welding. Accordingly, to achieve high-quality welding, it is necessary to deeply understand the weld pool formation processes.

2.1. Weld Pool Observation

Information on the flow field and temperature field is indispensable for understanding the heat transport process in the weld pool, but due to the difficulty in measurement, there are still few reports of these experimental measurement results.

Simultaneous measurement of both the keyhole behavior and its surrounding temperature field of the weld pool is indispensable for understanding the thermo-physical mechanism and also achieving the process control of KPAW. Zhang et al. used an infrared camera and a coupled charge device (CCD) camera to observe the temperature profile of the weld

pool in the vicinity of the keyhole and the keyhole behavior from below the base metal at the same time [13]. After image processing and calibration, the shapes and sizes of keyhole and weld pool as well as their relative positions were determined with temperature field.

Chen et al. observed the flow field on the surface of the weld pool employing a high-speed camera equipped with a laser light system and also the temperature field using an infrared thermal camera in VPPAW of aluminum alloys [14]. The formation mechanism of the keyhole weld pool at different welding positions was studied, especially for clarifying the effect of gravity on material flow, temperature field, and keyhole morphology. Based on the result of both calculation and experiment, the effect of gravity on the weld pool was found to be second only to shear force in all factors. Consequently, the heat and mass transport in the low-velocity region of the VPPA keyhole weld pool are thought to be readily influenced by the gravity.

In order to gain a deep understanding of the heat transport process in the weld pool, it is necessary to measure the flow field of the entire weld pool including the inside. For the first time, Nguyen et al. applied stereo synchronous imaging of tungsten tracer particles employing two sets of X-ray transmission systems to measure the 3D flow field inside the weld pool in KPAW [15]. The 2D convection on the surface of the weld pool was also measured by observing the motion of zirconia tracer particles. Based on this comprehensive measurement, the weld pool convection in the region behind the keyhole to the weld pool end was totally visualized. For discussing the heat transport process in the weld pool, the 2D temperature field on the top and bottom surfaces of the weld pool was also obtained by two-color pyrometry. A summary of the results of this comprehensive measurement is provided below.

Figure 2 shows weld pool images and 2D temperature fields on the top and bottom surfaces. On the top weld pool surface, the temperature was measured to be between 1718 K and 1795 K. The weld pool is divided into regions 1–3, according to the difference in temperature. The temperature reached 1795 K in region 2. On the bottom weld pool surface, the temperature was distributed between 1714 K and 1794 K. The temperature monotonically decreased from 1794 K around the keyhole to 1714 K at the weld pool end.

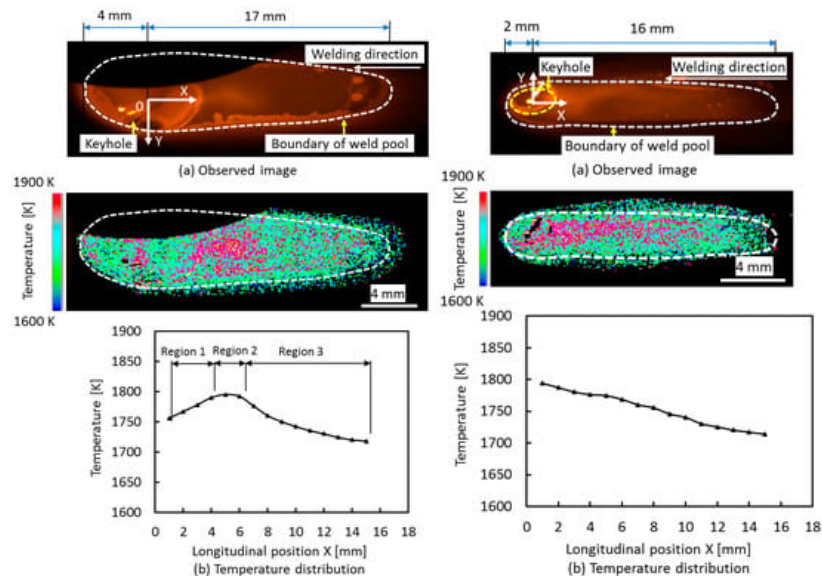


Figure 2. Observed image and temperature field on the surface of the weld pool. (a) Observed image; (b) temperature field on top (left figure) and bottom (right figure) surfaces [15].

Figure 3 shows 2D convective patterns on the top and bottom weld pool surfaces. On the top weld pool surface, the definition of each region is the same as that in **Figure 2**. In region 1, molten metal flowed from the keyhole to region 2 at a high temperature. It also flowed inward from the weld pool edge to the center of the weld pool. In region 3, the molten metal flowed in a forward direction from the weld pool end to region 2 at a high temperature. In region 2, the molten metal flows from regions 1 and 3 were merged. Zirconia particles were rotated due to this convective pattern. On the bottom weld pool surface, the molten metal flowed backward to the weld pool end. The maximum velocities of 0.53 m/s and 0.81 m/s were seen at $X = 2.0$ mm on the top surface and $X = 1.0$ mm on the bottom surface, respectively.

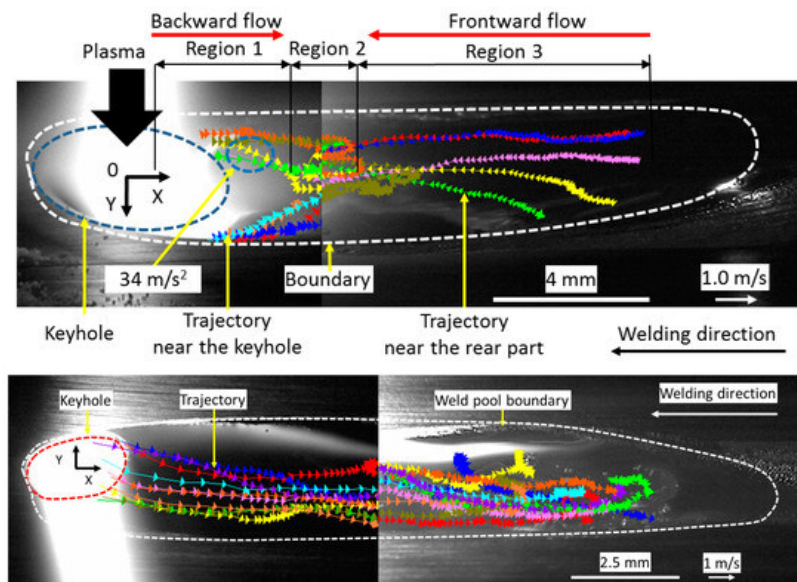


Figure 3. Convective pattern on top (upper figure) and bottom (lower figure) surfaces of the weld pool [15].

Figure 4 shows 3D convective patterns in the weld pool. The result showed that two eddy convective patterns in opposite directions were stably formed in the weld pool behind the keyhole. The maximum velocities for the molten metal flows near the top and bottom surfaces reached 0.35 and 0.30 m/s, respectively. The velocity of molten metal flow around the middle height decreased to 0.15 m/s.

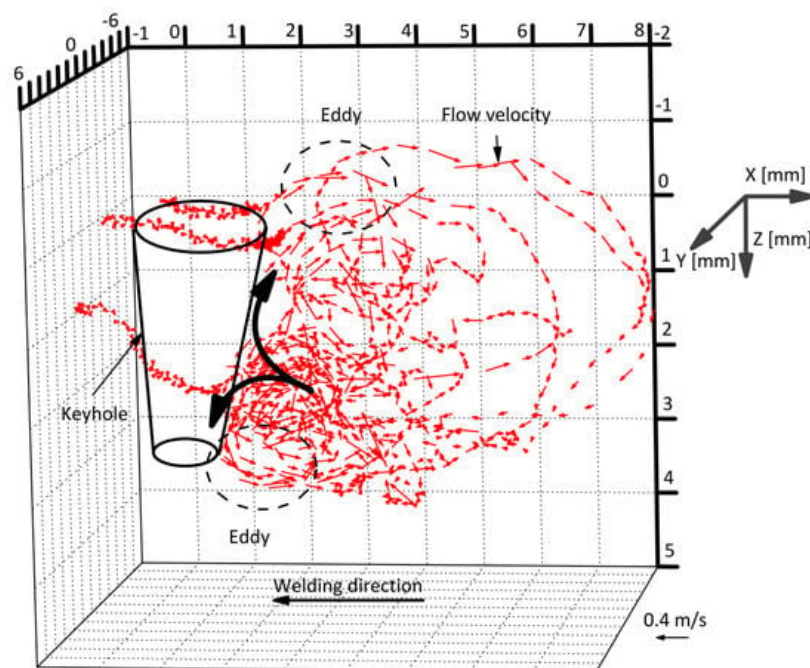


Figure 4. Three-dimensional convective patterns inside the weld pool in KPAW of stainless steel [15].

Xu et al. clarified the 3D keyhole detouring the flow inside the weld pool in VPPAW of an aluminum alloy employing two sets of X-ray transmission systems [16]. Furthermore, measurement of the surface flow of the weld pool at different regions of the keyhole was also carried out by observing tracers. As a result, it was shown that a thin liquid metal layer was formed on the keyhole boundary because of the high thermal conductivity of the aluminum alloy. Moreover, the liquid metal was mainly formed around the keyhole bottom. **Figure 5** shows 3D convective patterns in the weld pool. The liquid metal flowed upward and around the keyhole. The molten metal at the front wall of the keyhole around bottom detoured the keyhole backward. After that, it was blancheted into upward and downward flows, forming a vertical separation point. In addition, comparing with the stainless steel case [15], the flow velocity of VPPAW was found to be much smaller.

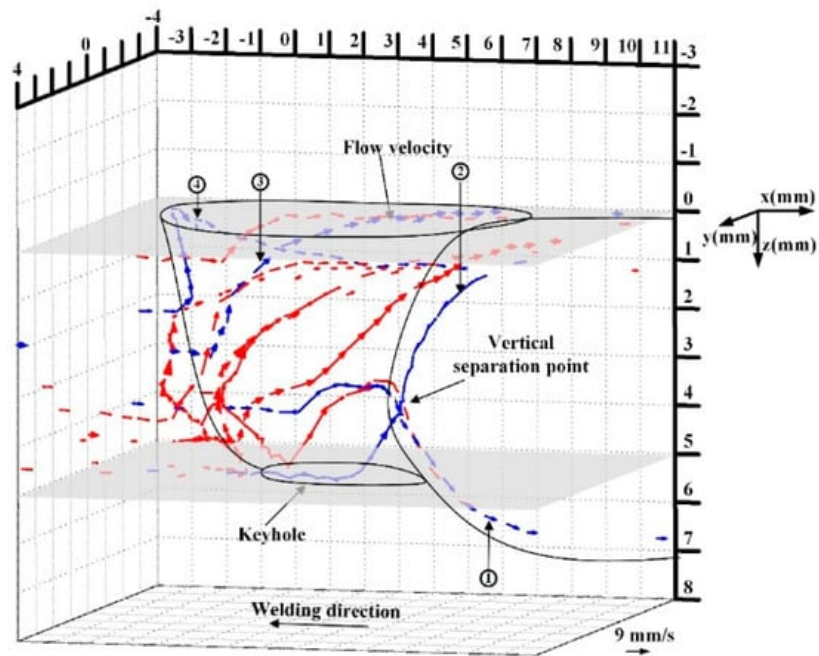


Figure 5. Three-dimensional keyhole detouring flow inside the weld pool in VPPAW of aluminum alloys [16].

2.2. Dominant Driving Force of Weld Pool Convection and Heat Transport Process in Weld Pool

Following the experimental results on KPAW of stainless steel [15], the dominant driving force of the weld pool convection in KPAW and its influence on the heat transport in the weld pool are discussed. As in the TIG welding case [17], the main driving forces of the weld pool convection in KPAW are buoyancy, Lorentz force, Marangoni force, and shear force especially in a quasi-steady state after stable open keyhole formation. **Figure 6** presents convections obtained by the measurement and also the estimated driving forces acting on each convection.

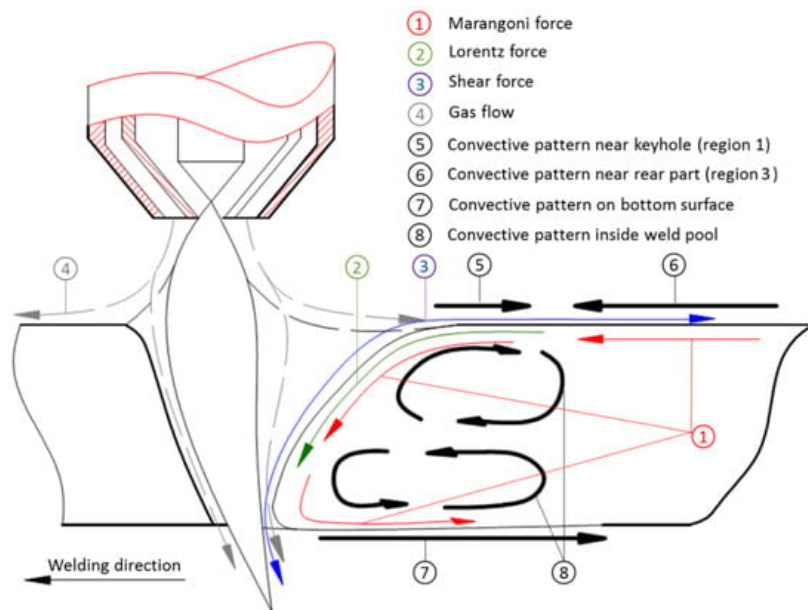


Figure 6. Schematic illustration of the main driving forces and convective patterns of the weld pool [15].

The buoyancy is weaker comparing with other forces and acts in an upward direction. Therefore, this force is considered to be negligible for weld pool formation.

The Lorentz force is generally in an inward and downward direction around the surface of the weld pool, since the current expands conically.

The shear force acting on the surface of the weld pool is composed of two forces. The first one is caused by plasma flowing along the top weld pool surface. The direction of this force is mainly upward and outward, inducing the clockwise convection around the top surface. The second one is caused by plasma flowing out downward through the keyhole exit. The direction of the force is downward, forming the counterclockwise convection around the bottom surface.

The Marangoni force is produced by the gradient of weld pool surface temperature. This force is generally directed from high temperature to low temperature in case of inert shielding gas. On the other hand, if an active gas like oxygen is mixed a little with the shielding gas, as expected in region 3, the force direction is reversed [18].

In region 1, the molten metal flowed backward from behind the keyhole to region 2 at a high temperature. The backward shear force was found to surpass the resultant Marangoni and Lorentz forces in the forward direction, therefore considered the dominant force. The maximum velocity appeared in the backside of the keyhole. It decreased as region 2 was approached.

In region 3, the molten metal flowed forward from the weld pool end to region 2 at a high temperature. The forward Marangoni force and backward shear force are considered to mainly act in this region, but the shear force is thought to be lower than the Marangoni force, because the velocity of plasma flow apart from the arc is largely decreased. Therefore, the molten metal flowed in the forward direction.

In region 2, the molten metal flowing from regions 1 backward and 3 forward merged.

On the bottom surface, the molten metal flowed backward from the keyhole to the weld pool end. The flow was accelerated by the downward shear force acting on the keyhole wall and backward Marangoni force on the bottom surface of the weld pool. Because of the acceleration by both forces, the flow velocity on the bottom surface was much higher than that on the top surface.

Inside the weld pool, two eddies were seen behind the keyhole. The flow in the upper eddy was in a clockwise direction. This eddy was accelerated by the upward and backward shear forces and the forward Marangoni force. Because the shear force is thought to be significantly larger than the Marangoni force, this eddy is mainly accelerated by the shear force. The flow in the lower eddy was essentially accelerated by the downward shear force and the downward and backward Marangoni forces. Therefore, this eddy flowed in a counterclockwise direction.

The formation process of the weld pool is also investigated in other arc welding processes through the measurement of velocity field of weld pool convection by tracer particle observation. For instance, the velocity field of the weld pool surface in TIGW was measured by Matsuda et al. [19]. They clarified that the velocity reached around 0.04 m/s around the foot point of the arc axis. Zong et al. measured the velocity field in GMAW and found that the range of velocity was about 0.15–0.20 m/s around the arc and 0.04 m/s around the weld pool end [20].

The weld pool formation process of KPAW is considered to be greatly different from those of TIGW and GMAW. The shear force, Lorentz force, and Marangoni force are known to play a major role as driving forces in TIGW and GMAW cases. In case of KPAW, the magnitudes of the Lorentz force and Marangoni force are predicted to have almost similar levels with those of TIGW and GMAW in the same current condition. On the other hand, the shear force is considered to be much larger compared with those of TIGW and GMAW due to the greater velocity of plasma flow [21], becoming the dominant force. Consequently, the velocity of convective flow surpasses those of TIGW and GMAW.

Wu et al. quantitatively analyzed the weld pool formation process through numerical simulation, presenting that after open keyhole formation, two convective eddies are produced behind the keyhole as in **Figure 7** [22]. In the weld pool, the molten metal was transported backward on the top surface by the upper eddy and backward at the bottom surface by the lower eddy. The calculated weld pool convections well agreed with the above observation.

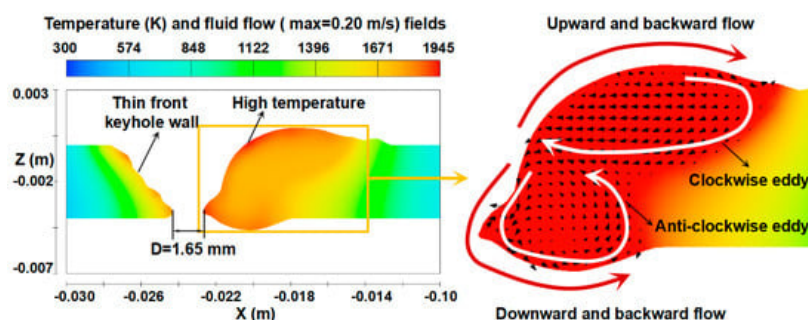


Figure 7. Calculated temperature and fluid flow fields [22].

Wu et al. carried out a numerical simulation to investigate the heat transport in a weld pool with an open keyhole in a quasi-steady state [23]. **Figure 8** shows the 3D temperature field of the weld pool. Although the weld pool temperature is found to increase around the keyhole, the maximum temperature is only 1857 K, which is slightly higher than the melting

point of steel. The heat flux from arc to base metal in the KPAW process is large due to the constricted arc, but the weld pool temperature is low. As presented by Nguyen et al. [15], the maximum surface temperature of the weld pool was approximately 1800 K, which was almost the same as that in the moving GTAW [24] and lower than that in the stationary GTAW [25]. The reasons to cause this low temperature can be explained as follows.

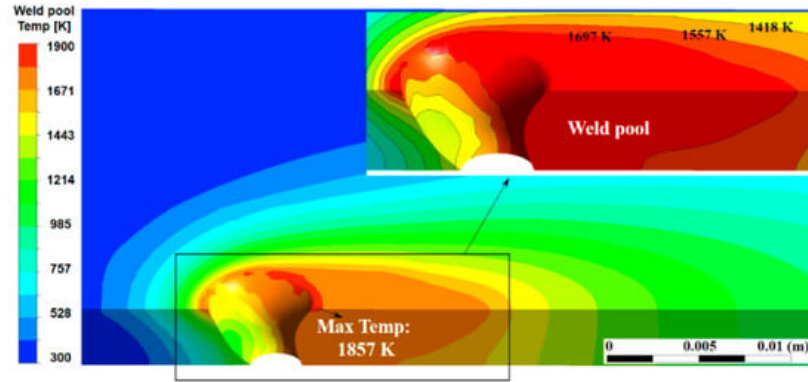


Figure 8. Three-dimensional temperature field in quasi-steady state [23].

Heat transport in the weld pool is carried out mainly by convection and conduction. The Peclet number is useful for discussing the dominant heat transport mechanism. As seen in **Figure 4** and **Figure 7**, two convective eddies were formed behind the keyhole consisting of the upper clockwise eddy and lower counterclockwise eddy. The molten metal was transported backward on the top and bottom surfaces. In the above result, a maximum velocity of 0.2884 m/s was seen in the weld pool. The calculated Peclet number from the velocity was approximately 319. Wang et al. calculated a Peclet number of the weld pool of about 77 in double electrodes TIGW [26]. Generally, when the Peclet number exceeds 10, the effect of heat transport due to convection is considered to be dominant. The result indicates that the heat transport by fluid flow is the dominant mechanism in the KPAW weld pool. As a result, the energy is not accumulated in the weld pool around the keyhole, leading to a lower weld pool temperature.

2.3. Effect of Torch Design and Operating Parameters

In the above paper [15], only one experimental condition was performed. However, it is considered that the driving force balance to govern the weld pool formation process significantly depends on the torch design and operating parameters. Because the shear force is strongly affected by the plasma flow field in the vicinity of the keyhole, the force balance is thought to greatly change depending on the keyhole shape. As shown in **Figure 4**, two large eddies are produced behind the keyhole in this experimental condition, because the plasma flow from the torch is separated to a downward flow outflowing to the bottom side through the keyhole exit and a horizontal and upward flow along the weld pool surface to form two opposite shear forces. For example, in the case of higher plasma gas flow rate or current, the arc pressure acting on the surface of the weld pool is enhanced, leading to a wider keyhole diameter and a steeper keyhole wall. In this case, the downward flow through the keyhole exit might be larger than the horizontal and upward flow. The formation of eddies is expected to be affected by an increase in shear force, making the lower eddy relatively larger. It also causes a variation in the heat transport in the weld pool. Nguyen et al. studied the effect of plasma gas flow rate [27], welding current [28], and also the shielding gas composition [29], and Xu et al. clarified the effects of electrode setback [30] and plate thickness [31] in VPPAW of aluminum alloys. Those studies used the same comprehensive experimental approach.

Figure 9 shows 3D convective patterns inside the weld pool for different plasma gas flow rates [27]. The weld bead appearances and cross sections of the weld beads were already presented in **Figure 4**. As the plasma gas rate is increased, a penetrated keyhole is formed. The counterclockwise eddy inside the weld pool becomes large and then dominant. The backward flow on the top surface is weakened, while the inward flow is induced by the teardrop-shaped top weld pool profile. According to the dominant counterclockwise eddy inside the weld pool, the molten metal temperature at the lateral sides of the top weld pool is low.

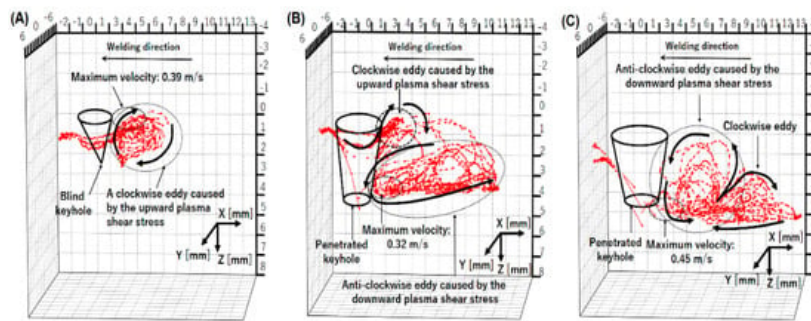


Figure 9. Three-dimensional convective patterns inside the weld pool for different plasma gas flow rates: (A) 0.7 L/min; (B) 1.7 L/min; (C) 3.0 L/min [27].

As described above, convection is the dominant mechanism for the heat transport inside the weld pool in KPAW. The strong counterclockwise eddy formed behind the keyhole and the weak backward flow on the top surface of the weld pool produce the uneven energy distribution between the top and bottom surfaces. The strong inward flow causes the uneven energy distribution between the lateral sides and centerline of the top weld pool. All these reasons contribute to the undercut formation at the top surface.

Figure 10 shows 3D convective patterns inside the weld pool for different currents [28]. The weld bead appearances and cross sections of the weld beads have already been presented in **Figure 5**. In case of a low current of 90 A, an open keyhole was formed with a smaller diameter on the bottom surface than that on the top surface. This is due to the insufficient penetration ability and is considered to produce a strong upward shear force. Therefore, the upper eddy grew up more compared with the lower one. On the other hand, in case of a high current of 150 A, an open keyhole was formed with a large diameter on the bottom surface. The lower eddy was enhanced due to a strong downward shear force. This relative magnitude of the two eddies is thought to significantly affect the heat transport in the weld pool and also the welding defect occurrence. The stronger upper eddy due to the insufficient heat input might cause an undercut and high reinforcement on the top surface. On the contrary, the stronger lower eddy leads to deeper penetration by the large heat transport in a downward direction. However, if the downward heat transport is excessive, it leads to welding defects such as concaves on the top surface and burn-throughs on the bottom surface. Consequently, it is considered that when the arc has sufficient penetration ability to the base metal, the relative magnitude of the two eddies should be suitably controlled for achieving the larger counterclockwise eddy and smaller clockwise eddy, which enables achievement of a stable and high-quality welding preventing welding defect occurrence, as in the optimal current of 120 A in this experiment.

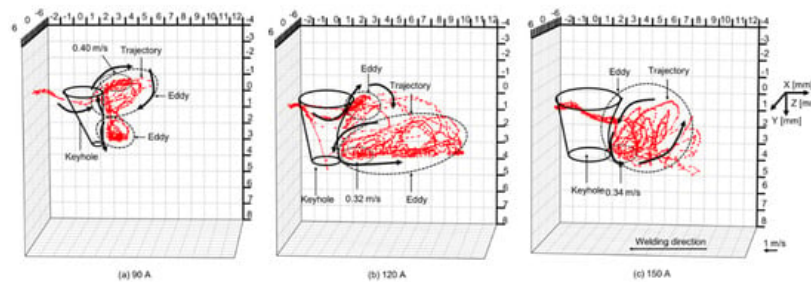


Figure 10. Three-dimensional convective patterns inside the weld pool for different currents [28].

Figure 11 shows 3D convective patterns inside the weld pool for different shielding gas compositions [29]. The weld bead appearances and cross sections of the weld beads have already been presented in **Figure 6**. It was presented that in the case of pure Ar shielding gas, the molten metal flowed upward behind the keyhole. In the case of Ar with 0.5% O₂ shielding gas, the flow direction became downward behind the keyhole. The molten metal flow in the weld pool is varied depending on the keyhole shape, for example, by the keyhole diameter and keyhole wall inclination angle. The keyhole diameter is large on the top side and small on the bottom side in the pure Ar case, but it is smaller on the top side and larger on the bottom side in the Ar mixed with 0.5% O₂ case. The magnitude and direction of the shear force are influenced by this difference. As a result, it was found that the addition of a small amount of oxygen into Ar shielding gas assuming shielding failure strongly affected the heat transport process. It is also implied that narrow and deep penetration can be achieved by mixing oxygen slightly such as in the AA-TIG welding process [32]. This mechanism is considered to be related primarily to the variation in shear force because of different keyhole shape formation due to change in the surface tension rather than the variation in the magnitude and direction of the Marangoni force.

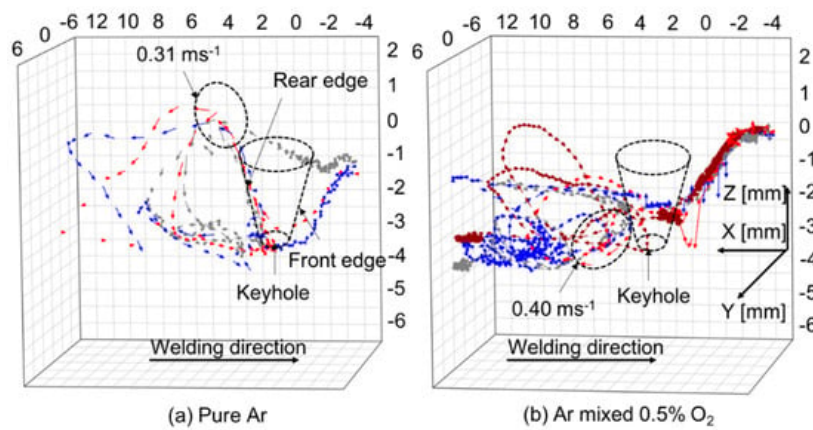


Figure 11. Three-dimensional convective patterns inside the weld pool for different shielding gas compositions [29].

2.4. Effect on Microstructure of Solidified Metal in Welded Joint

As mentioned above, the heat and mass transport within the weld pool governs the formation of the temperature field in the weld pool and therefore has a strong influence on the microstructure of solidified metal, mainly according to a temperature history during the cooling process, thus affecting mechanical properties of the welded joint.

There are many previous studies on the microstructure in KPAW. For example, microstructures when applying KPAW to various materials have been reported, such as duplex stainless steel [33][34], Inconel [35], aluminum alloy [36], and titanium alloy [37]. Comparative studies with microstructures in other arc welding processes have also been conducted. Gupta et al. compared the welded joints prepared by a single-pass KPAW and multi-pass GATAW of M 250 (Maraging steel) with a thickness of 8 mm, showing improved mechanical and metallurgical properties for KPAW in comparison to those for GTAW [38]. Welding parameters such as current waveform also affect the microstructure [35][37]. Kumar et al. found that pulse current helps in grain refinement, which leads to a higher ultimate tensile strength of the welded joints [37]. Large current and high peak current lead to more heat and a longer cooling time, resulting in coarse grain. When the pulse rate is increased, the tensile strength is also increased.

The above studies basically demonstrate the relationship between welding conditions and microstructures experimentally. Although these results are very useful industrially, its mechanism has not been fully elucidated academically. In particular, there are very few studies on the formation process of the microstructure in welded joints based on quantitative discussions of heat and mass transport within the weld pool. Yan et al. investigated the gravity effect on the mechanical property of VPPAW of aluminum alloys at vertical and horizontal positions [39]. Microstructures and residual stress in the welded joint for vertical-up welding were symmetrical. This is in contrast to horizontal welding, which tends to have asymmetric and inhomogeneous microstructures that lead to poor mechanical properties. In the upper side of welded joints for horizontal welding, larger grain sizes brought about lower hardness and lower tensile strength. The difference in the mechanical properties between bilateral sides was suggested to be caused by gravity driving the melting metal flow. After that, Liu et al. carried out the measurements of temperature field and velocity field on the weld pool surface of VPPAW at different positions to discuss the effect of heat and mass transport in the weld pool on microstructure and also mechanical properties of the welded joint through the gravity force [40]. From the measurement, they found that the asymmetric flow of molten metal under the influence of gravity is the main factor leading to uneven temperature distribution and asymmetric grain distribution in the weld pool. Furthermore, Xu et al. clarified the relationship between the microstructure of the welded joint and the heat and mass transport in VPPAW of thick aluminum alloy plates at a flat position by combining in situ three-dimensional X-ray imaging and multi-physics modeling [31]. **Figure 12** shows the microstructure and crystal size of the weld bead. It was concluded that the large crystal size observed in the lower layer of the weld is partly caused by heat treatment from the upper layer of the thick plate. An eddy with a high flow velocity to the rear of the weld pool destroys the crystal-growth process, and this is considered to be one of the reasons for fine crystals appearing in the upper part of the weld.

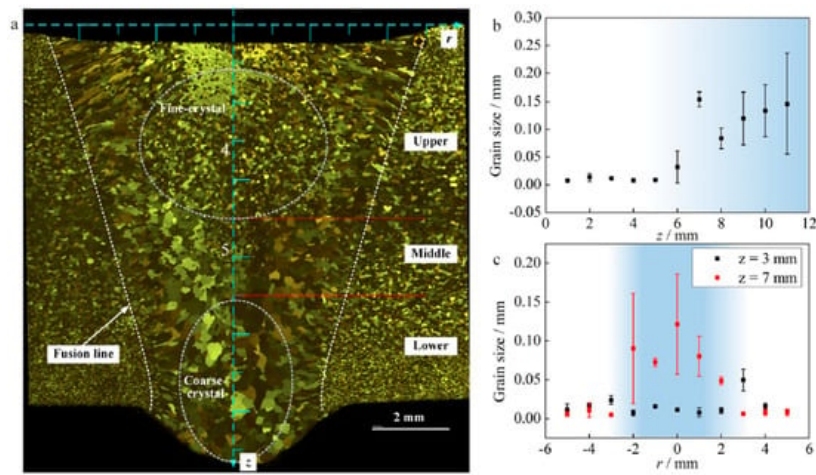


Figure 12. Microstructure and crystal size of the weld bead in VPPAW of a thick aluminum plate [31].

In this way, it has been found that the formation of the microstructure is greatly affected by the flow of the weld pool and the accompanying heat transport. Also, in KPAW, a filler wire is often used when the base material plate thickness is large. Especially when the chemical composition of this filler wire is different from that of the base metal, non-uniform element distribution tends to occur within the weld pool due to weld pool flow [41], which is also thought to affect the formation of the microstructure. Elucidation of the influence of the weld pool formation process on the formation of the microstructure of the solidified metal in the welded joint is still insufficient and remains a future work.

References

- Lucas, W. TIG and Plasma Welding, 3rd ed.; Abington Publishing: Cambridge, UK, 2008; pp. 80–108.
- Murphy, A.B.; Lowke, J.J. Heat Transfer in Arc Welding. In Handbook of Thermal Science and Engineering; Springer: New York, NY, USA, 2018; pp. 2657–2727.
- Li, Z.; Wu, D.; Tashiro, S.; Tanaka, M.; Xin, J.; Wang, H.; Hua, X. Influence mechanism of metal vapor in plasma arc lap welding. *Weld. J.* 2022, 101, 161s–171s.
- Nguyen, H.L.; Van Nguyen, A.; Duy, H.L.; Nguyen, T.-H.; Tashiro, S.; Tanaka, M. Relationship among Welding Defects with Convection and Material Flow Dynamic Considering Principal Forces in Plasma Arc Welding. *Metals* 2021, 11, 1444.
- Sakuramoto, Y.; Wada, K.; Kanemaru, S.; Kamei, T. Application of Plasma Welding Process for Manufacturing of Stainless Steel Cylindrical Vessel. In TAIYO NIPPON SANSO Technical Report; Taiyo Nippon Sanso: Tokyo, Japan, 2013; Volume 32, pp. 33–34. (In Japanese)
- Wang, L.L.; Lu, F.G.; Wang, H.P.; Murphy, A.B.; Tang, X.H. Effects of shielding gas composition on arc profile and molten pool dynamics in gas metal arc welding of steels. *J. Phys. D Appl. Phys.* 2014, 47, 465202.
- Martikainen, J.K.; Moisio, T.J.I. Investigation of the effect of welding parameters on weld quality of plasma arc keyhole welding of structural steels. *Weld. J.* 1993, 72, 329s–340s. Available online: https://app.aws.org/wj/supplement/WJ_1993_07_s329.pdf (accessed on 11 March 2024).
- Banas, C.M. Electron Beam, Laser Beam and Plasma Arc Welding Studies NASA Contractor Report NASA-CR-132386; United Aircraft Research Laboratories: East Hartford, CT, USA, 1974.
- Vilkas, E.P. Plasma arc welding of exhaust pipe system components. *Weld. J.* 1991, 70, 49–52.
- Wu, C.S.; Wang, L.; Ren, W.J.; Zhang, X.Y. Plasma arc welding: Process, sensing, control and modeling. *J. Manuf. Process.* 2014, 16, 74–85.
- Liu, Z.M.; Cui, S.L.; Luo, Z.; Zhang, C.Z.; Wang, Z.M.; Zhang, Y.C. Plasma arc welding: Process variants and its recent developments of sensing, controlling and modeling. *J. Manuf. Process.* 2016, 23, 315–327.
- Sahoo, A.; Tripathy, S. Development in plasma arc welding process: A review. *Mater. Today Proc.* 2021, 41, 363–368.
- Zhang, G.; Wu, C.S.; Liu, Z. Experimental observation of both keyhole and its surrounding thermal field in plasma arc welding. *Int. J. Heat Mass Transf.* 2014, 70, 439–448.
- Chen, S.; Liu, J.; Jiang, F.; Xu, B.; Zhang, G.; Li, B. Gravity effects on temperature distribution and material flow in the keyhole pool of VPPA Al welding. *Int. J. Heat Mass Transf.* 2022, 191, 122823.

15. Nguyen, A.V.; Tashiro, S.; Bui, H.V.; Tanaka, M. Experimental investigation on the weld pool formation process in plasma keyhole arc welding. *J. Phys. D Appl. Phys.* 2018, 51, 015204.
16. Xu, B.; Chen, S.; Tashiro, S.; Jiang, F.; Nguyễn, V.A.; Tanaka, M. Material flow analyses of high-efficiency joint process in VPPA keyhole flat welding by X-ray transmission system. *J. Clean. Prod.* 2020, 250, 119450.
17. Tanaka, M.; Lowke, J.J. Predictions of weld pool profiles using plasma physics. *J. Phys. D Appl. Phys.* 2007, 40, R1–R23.
18. Lu, S.; Fujii, H.; Sugiyama, H.; Tanaka, M.; Nogi, K. Effects of oxygen additions to argon shielding gas on GTA weld shape. *ISIJ Int.* 2003, 43, 1590–1595.
19. Matsuda, S.; Tanahara, Y. Effect of magnetic field on flows and temperature distribution of molten pool in electromagnetic controlled molten pool welding process. *Q. J. Jpn. Weld. Soc.* 2015, 84, 244–250.
20. Zong, R.; Chen, J.; Wu, C.S.; Padhy, G.K. Influence of molten metal flow on undercutting formation in GMAW. *Sci. Technol. Weld. Join.* 2016, 234, 169–176.
21. Schnick, M.; Füssel, U.; Spille-Kohoff, A. Numerical Investigations of the Influence of Design Parameters, Gas Composition and Electric Current in Plasma Arc Welding (PAW). *Weld. World* 2010, 54, R87–R96.
22. Wu, D.; Nguyen, A.V.; Tashiro, S.; Hua, X.; Tanaka, M. Elucidation of the weld pool convection and keyhole formation mechanism in the keyhole plasma arc welding. *Int. J. Heat Mass Transf.* 2019, 131, 920–931.
23. Wu, D.; Tashiro, S.; Hua, X.; Tanaka, M. Analysis of the energy propagation in the keyhole plasma arc welding using a novel fully coupled plasma arc-keyhole-weld pool model. *Int. J. Heat Mass Transf.* 2019, 141, 604–614.
24. Sato, T.; Okubo, A.; Oji, T.; Hirata, Y. Measurement of molten pool temperature distribution by UV thermal radiation. *Weld. Int.* 1998, 12, 627–634.
25. Tanaka, M.; Terasaki, H.; Ushio, M.; Lowke, J.J. Numerical Study of a Free-burning Argon Arc with Anode Melting. *Plasma Chem. Plasma Process.* 2003, 23, 585–606.
26. Wang, X.; Fan, D.; Huang, J.; Huang, Y. Numerical simulation of arc plasma and weld pool in double electrodes tungsten inert gas welding. *Int. J. Heat Mass Transf.* 2015, 85, 924–934.
27. Nguyen, A.V.; Wu, D.; Tashiro, S.; Tanaka, M. Undercut Formation Mechanism in Keyhole Plasma Arc Welding. *Weld. J.* 2019, 98, 204s–212s. Available online: <https://s3.amazonaws.com/WJ-www.aws.org/supplement/2019.98.018.pdf> (accessed on 11 March 2024).
28. Nguyen, A.V.; Tashiro, S.; Ngo, M.H.; Bui, H.V.; Tanaka, M. Effect of the eddies formed inside a weld pool on welding defects during plasma keyhole arc welding. *J. Manuf. Process.* 2020, 59, 649–657.
29. Nguyen, A.V.; Tashiro, S.; Ngo, M.H.; Lee, A.H.; Bui, H.V.; Tanaka, M. Influence of shielding gas composition on molten metal flow behavior during plasma keyhole arc welding process. *J. Manuf. Process.* 2020, 53, 431–437.
30. Xu, B.; Chen, S.; Tashiro, S.; Jiang, F.; Tanaka, M. Physical mechanism of material flow in variable polarity plasma arc keyhole welding revealed by in situ x-ray imaging. *Phys. Fluids* 2021, 33, 017121.
31. Xu, B.; Tashiro, S.; Tanaka, M.; Jiang, F.; Chen, S. Physical mechanisms of fluid flow and joint inhomogeneity in variable-polarity plasma arc welding of thick aluminum alloy plates. *Phys. Fluids* 2021, 33, 087103.
32. Fujii, H.; Sato, T.; Lu, S.; Nogi, K. Development of an advanced A-TIG (AA-TIG) welding method by control of Marangoni convection. *Mater. Sci. Eng. A* 2008, 495, 296–303.
33. Urena, A.; Otero, E.; Utrilla, M.V.; Munez, C.J. Weldability of a 2205 duplex stainless steel using plasma arc welding. *J. Mater. Process. Technol.* 2007, 182, 624–631.
34. Migiakis, K.; Daniolos, N.; Papadimitriou, G.D. Plasma Keyhole Welding of UNS S32760 Super Duplex Stainless Steel: Microstructure and Mechanical Properties. *Mater. Manuf. Process.* 2010, 25, 598–605.
35. Prasad, K.S.; Rao, C.S.; Rao, D.N. Optimization of fusion zone grain size, hardness, and ultimate tensile strength of pulsed current micro plasma arc welded Inconel 625 sheets using genetic algorithm. *Int. J. Adv. Manuf. Technol.* 2016, 85, 2287–2295.
36. Cai, D.; Han, S.; Yan, D.; Luo, Z.; Wang, H.; Zhang, Y. Microstructure and fatigue behavior of variable polarity plasma arc welded Al-6.2Mg alloys. *J. Mater. Process. Technol.* 2019, 269, 128–134.
37. Kumar, A.S.; Rao, T.V.H.; Rao, V.V.S.K.; RamaKanth, R.T. Optimizing pulsed current micro plasma arc welding parameters to maximize ultimate tensile strength of titanium (Ti-6Al-4V) alloy using Dragon fly algorithm. *Mater. Today Proc.* 2020, 27, 2086–2090.
38. Gupta, R.; Reddy, R.; Mukherjee, M.K. Key-Hole Plasma Arc Welding Of 8 Mm Thick Maraging Steel—A Comparison with Multi- Pass Gtaw. *Weld. World* 2012, 56, 69–75.

39. Yan, Z.; Chen, S.; Jiang, F.; Zhang, W.; Huang, N. Study and optimization against the gravity effect on mechanical property of VPPA horizontal welding of aluminum alloys. *J. Manuf. Process.* 2019, 46, 109–117.
 40. Liu, J.; Jiang, F.; Chen, S.; Wang, K.; Zhang, G.; Xu, B.; Cheng, W.; Ma, X. Cross-scale process quality control of variable polarity plasma arc welding based on predefined temperature field. *J. Mater. Res. Technol.* 2023, 26, 5347–5359.
 41. Wu, D.; Ishida, K.; Tashiro, S.; Nomura, K.; Hua, X.; Ma, N.; Tanaka, M. Dynamic keyhole behaviors and element mixing in paraxial hybrid plasma-MIG welding with a gap. *Int. J. Heat Mass Transf.* 2023, 200, 123551.
-

Retrieved from <https://encyclopedia.pub/entry/history/show/127043>